Microscopic structure of stacking faults in $Sr_2NaNb_5O_{15}$

Robin Sjökvist,[1] Yining Xie,[1] Zabeada Aslam,[2,3] Andy P. Brown,[2,3] Nicholas C. Bristowe,[4] Mark S. Senn,[5] and Richard Beanland[1,*]

[1]*Department of Physics, University of Warwick, Coventry CV4 7AL, United Kingdom*
[2]*School of Chemical and Process Engineering, University of Leeds, Leeds LS2 9JT, United Kingdom*
[3]*Bragg Centre for Materials Research, University of Leeds, Leeds LS2 9JT, United Kingdom*
[4]*Centre for Materials Physics, Durham University, Durham DH1 3LE, United Kingdom*
[5]*Department of Chemistry, University of Warwick, Coventry CV4 7AL, United Kingdom*

(Received 10 November 2025; revised 18 February 2026; accepted 22 April 2026; published 8 June 2026)

Stacking faults and other topological defects in ferroics can have a significant influence on the electronic and mechanical properties of the material. Here, regular stacking faults in the tetragonal tungsten bronze material $Sr_2NaNb_5O_{15}$ are investigated through transmission electron microscopy, symmetry mode analysis, and machine-learned force-field calculations. It is shown that the faults, with a fault vector of $\frac{1}{4}[\bar{2}12]_o$, annihilate in sets of four in the material, owing to the ¼ unit cell displacement along the b-axis. The four resulting domains emerge as four possible directions of the S_3 order parameter, related to NbO_6 octahedral tilts in the material. Force-field calculations reveal that the stacking faults are likely placed at positions where the octahedra in neighboring domains have similar magnitudes of rotation, and that the estimated stacking fault energy is 46 mJ/m^2. The investigation shows that the stacking faults have a local effect on the in-plane polar mode present in the structure, and therefore could affect the ferroelectric properties.

DOI: 10.1103/snjy-yzgq

I. INTRODUCTION

The tetragonal tungsten bronze (TTB) $Sr_2NaNb_5O_{15}$ (SNN) is currently being investigated as a modern ferroelectric material with application as a dielectric in high-temperature capacitors [1–4]. Its high and stable dielectric response across a large temperature range makes it an attractive alternative to polymer-based dielectrics and is a necessity for efficient energy storage and retention at elevated temperatures [5]. Another benefit is that SNN is Pb and Bi-free, making it more compatible with current Ni-based multilayer capacitor electrode technology, unlike many other ceramic oxide ferroelectrics [6,7].

The TTBs have the general formula $(A1)_2(A2)_4C_4(B1)_2(B2)_8O_{30}$, and constitute the second largest group of ferroelectric materials after the perovskites [7]. The large unit cell, in combination with the many different sites suitable for different ionic valencies, makes the basic TTB structure incredibly versatile. In the case of SNN, the A-sites are occupied by Sr and Na, while the B-sites are occupied by Nb, and the C-site is vacant. The crystal structure has been recently solved through the means of a combination of Transmission Electron Microscopy (TEM), powder X-ray Diffraction (XRD), and neutron diffraction, where it was established that SNN at room temperature adopts an incommensurate, octahedrally tilted structure which approximates closely to an orthorhombic *Ama2* phase [8]. The structure exhibits an out-of-plane polarization, owing to the displacement of Nb atoms within NbO_6 octahedra, which results in the ferroelectric properties. *Ama2* relates to the high-temperature tetragonal aristotype *P4/mbm* phase via the basis transformation $\{(1, -1, 0), (2, 2, 0), (0, 0, 2)\}$, and the same crystal structure has also been suggested for the related TTBs $Ba_{0.61}Pb_{0.39}Nb_2O_6$ and $Sr_{0.61}Ba_{0.39}Nb_2O_6$ [9,10]. In Fig. 1(a), the *Ama2* structure is drawn in the $[001]_o = [001]_t$ projection (o = orthorhombic, t = tetragonal), while the same structure is shown in the $[100]_o = [1\bar{1}0]_t$ direction in Fig. 1(b).

It is well known that the micro- and nanostructure of materials will ultimately affect the device performance, and the presence of stacking faults and other planar defects in ferroelectrics has been shown to affect, for example, the polarization response [11,12]. Dark field (DF) TEM imaging has shown that SNN contains a high density of planar faults that tend to lie on $(010)_o$ planes and have provisionally been identified as anti-phase boundaries (APBs) [8]. The faults are expected to arise as a way to accommodate the strain arising from the mismatch between the commensurate and incommensurate lattices during growth. Due to the potential impact on the dielectric properties of these planar defects in SNN, a full characterization of the structure of the planar faults, as well as an investigation of the symmetry relationship between the domains they form, is warranted.

In this paper, transmission electron microscopy and electron diffraction have been used to reveal and image these planar crystallographic defects in SNN. By using selected area diffraction on individual grains, domains in the structure can be found and properly described, while the utilization of high-resolution TEM allows a demonstration of the nature of

*Contact author: r.beanland@warwick.ac.uk

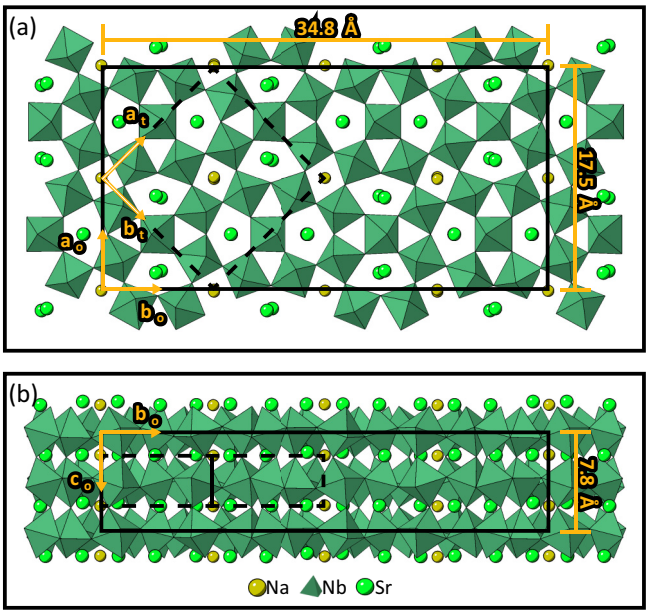

FIG. 1. Crystal structure projections. The orthorhombic Ama2 structure (solid line) viewed along (a) $[001]_o$ and (b) $[100]_o$, with the superimposed extent of the tetragonal aristotype P4/mbm structure (dashed line) viewed along (a) $[001]_t$ and (b) $[1\bar{1}0]_t$. For simplicity, we display the structure with 100% occupation of the Sr and Na on the two different A-sites. The O atoms situated at the corners of the Nb-octahedra have been omitted for clarity.

the defects. The investigation shows that the planar defect is a type of stacking fault with a preferred habit plane perpendicular to the *b*-axis of the orthorhombic *Ama2* structure, with a fault vector $\frac{1}{4}[\bar{2}12]_o$. DF TEM imaging reveals that the stacking faults always merge in sets of four, similar to that observed for the related TTBs BNN and SKN ($Ba_2NaNb_5O_{15}$ and $Sr_2KNb_5O_{15}$, respectively) [13]. Through the use of ISODISTORT [14,15], it was found that the stacking faults can be understood to arise due to the different symmetry-allowed order parameter directions (OPDs) of the S_3 order parameter, which is related to cooperative tilting of NbO_6 octahedra, expressed as phase shifts. The faults are then expected to form in regions where the displacive modulation of the NbO_6 octahedra tends to zero, as this would minimize the energy penalty. Based on this assumption, a structure encompassing four faults was constructed and simulated using force-fields [machine-learned from density functional theory (DFT)], revealing a minimal energy cost of $46 \pm 1\,\mathrm{mJ/m^2}$. Finally, we speculate on the implications of the faults, and show through symmetry mode analysis, atomic displacements, and DF TEM that the presence of the faults has an effect on the ferroelectric properties of SNN.

II. METHODS

Ceramic powders of SNN were prepared following an established synthesis route [6,8]. To prepare samples for transmission electron microscopy, the ceramic was ground with fine (<10 μm) aluminium powder at a 1:10 ratio and placed in aluminium foil. The folded foil was subsequently pressed using cold rollers, producing a thin, solid aluminium sheet containing particles of ceramic, which was thinned through mechanical grinding and polishing, mounted to a Cu TEM support using epoxy resin, and thinned to transparency using Ar^+ ion milling (Gatan PIPS II). High-resolution and dark field/bright field transmission electron microscopy was carried out using a JEOL 2100 LaB_6 TEM operated at 200 keV. Atomic resolution annular dark field (ADF) scanning transmission electron microscopy (STEM) was carried out in an aberration-corrected JEOL ARM200F FEG TEM operated at 200 keV (20 mrad convergence semi-angle and 55–180 mrad detector semi-angle). 4D-STEM was carried out in a TESCAN Tensor 100 keV FEG TEM (2 mrad convergence semi-angle and 1.66 nm probe size).

In order to tractably, but accurately, simulate the stacking faults in this complex material with a large unit cell, machine-learned force-fields were constructed from DFT (DFT details can be found elsewhere [8]) using the kernel-based "on-the-fly" approach adopted in the VASP software [16,17]. For simplicity, SNN was modeled with 100% occupation of Sr and Na on the two different A-sites (which was previously found to provide good agreement with experiment) [8]. The reference configurations used to build the force field were generated on-the-fly during a DFT molecular dynamics simulation in which the *Cc* phase (which is similar to the room-temperature *Ama2* structure but with an additional in-plane polarization, observed to be the ground state of SNN [8]) was slowly warmed up to around 1000 K. The accuracy of the force field was tested against DFT results on structures not explicitly in the training set. Since symmetry breaking from the stacking faults would likely relax the *Ama2* faulted structure to *Cc* (or other low-energy phases) in subsequent 0 K structural relaxation calculations, the *Cc* phase was used as a model system to simulate the stacking faults. More details about the machine-learned force fields can be found in Supplemental Material [18].

III. RESULTS

Figure 2(a) illustrates several aspects of the microstructure of SNN. The dark field (DF) transmission electron micrograph highlights two domains of different orientation, with corresponding diffraction patterns in Figs. 2(b) and 2(c), respectively. The domain corresponding to Fig. 2(b) appears dark and is imaged in the $[010]_o$ zone axis. It shares a curved and uneven border with the second domain, which appears bright, and the diffraction pattern of Fig. 2(c) shows that it is aligned to the $[100]_o$ zone axis. The orientational relationship between adjacent domains is therefore that of a 90-degree rotation about $[001]_o$, i.e., orthorhombic twinning. In Fig. 2(c), a spot of the type $\frac{1}{4}112_t = 011_o$, used for the dark field imaging in Fig. 2(a), is indicated by the yellow circle. It is worth mentioning that the spot is displaced slightly from its ideal ¼ index along the orthorhombic b direction, owing to the slightly incommensurate nature of the structure as reported previously [8]. Most notably, these imaging conditions allow the visualization of bright and dark lines throughout the $[100]_o$ region in Fig. 2(a), corresponding to planar faults in the structure.

Upon closer inspection of the planar faults present in Fig. 2(a), it can be seen that, although they often originate at

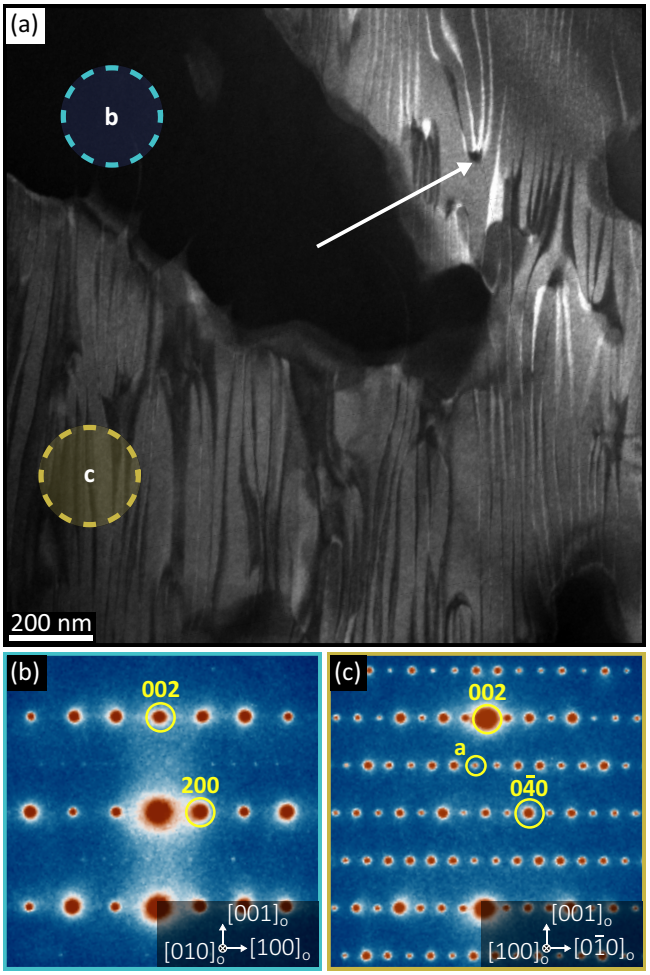

FIG. 2. (a) Dark field micrograph, showing two neighboring 90° domains, with corresponding diffraction patterns (b) and (c) as labeled in the figure. The spot used when recording the dark field image presented in (a) is indicated by the yellow circle labeled "a" in (c), and has the indices 011_o.

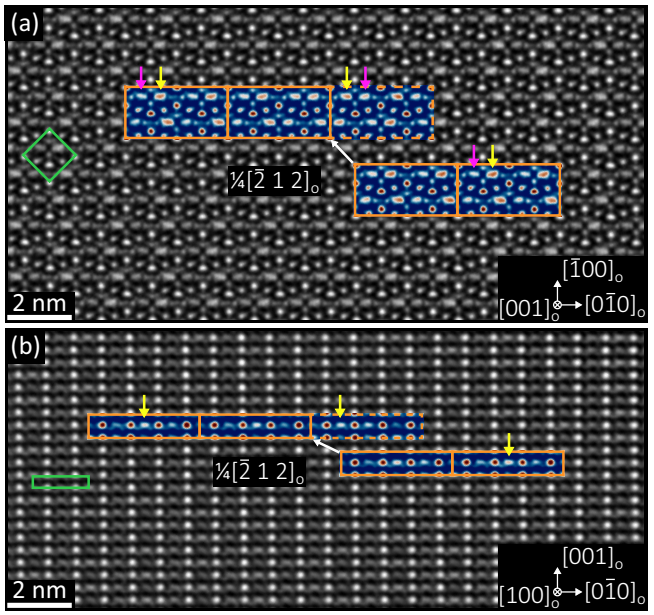

FIG. 3. HRTEM micrographs of stacking faults. (a) The structure is imaged in the $[001]_o$ direction, giving the in-plane contributions to the fault vector. Yellow and magenta arrows indicate a couple of the features that invert in contrast when crossing the fault. Introducing the fault vector restores the contrast. (b) The structure imaged in the $[100]_o$ direction, giving the out-of-plane contribution to the fault, and a final fault vector of $\frac{1}{4}[\bar{2}12]_o$. The yellow arrow indicates a specific feature of high contrast that shifts when crossing the fault. Its original position is restored by introducing the fault vector. The projection of the aristotype TTB unit cell is indicated in green in both panels. Bragg-filtering is used to improve contrast, as shown in Supplemental Material Fig. S2 [18].

the border between the twin domains, they tend to run parallel to each other along the c-axis of the orthorhombic cell and only terminate by merging in sets of four. The merging points are expected to be line defects going into the plane (along $[100]_o$), and one such merging point is indicated by a white arrow in the figure. Similar to the case of hexagonal $ErMnO_3$ where domain walls always meet in sets of six [22], this indicates there is a topological constraint on these crossing points that is determined by the crystallography of the material, as will be discussed later.

To obtain a better understanding of the atomistic structure of the faults, the material was also imaged using high-resolution transmission electron microscopy (HRTEM). Unlike aberration-corrected scanning transmission electron microscopy (ac-STEM), these images are dominated by phase contrast that results from the interference of the electron wave passing through the specimen. As such, bright and/or dark spots cannot be associated with individual atom columns, and the image does not provide atomic resolution. Nevertheless, the periodicity and symmetry of the image are constrained to match that of the projected crystal potential. Importantly for this material, the contrast is exquisitely sensitive to small atomic displacements, including those of light atoms like oxygen, meaning that the periodicity of the *Ama2* structure is readily apparent.

Figure 3(a) shows an HRTEM image of SNN viewed along the c-axis of the orthorhombic unit cell [same orientation as Fig. 1(a)]. Here, the fault is essentially invisible to the uninformed eye but runs vertically through the centre of the image. To demonstrate its presence, two unit cells are outlined in orange on either side of the fault, and the resulting fault vector is indicated by a white arrow. A color scheme is also applied in order to increase the visibility of the features in the unit cells. Looking at the two unit cells drawn to the left of the fault, it can be seen that the contrast of some of the features in the unit cells, highlighted by magenta and yellow arrows, follows a pattern of alternating contrast. Continuing to the dashed "unit cell" drawn in the same row, it can be seen that here the contrast of these features is reversed, indicating that this no longer shows the same unit cell setting. If, however, a shift in the unit cell origin is introduced by the fault vector (described below), the original contrast pattern can be found in the unit cells drawn to the right of the fault. Since the image is sensitive only to projected structure, any shift along the $[001]_o$ viewing direction, i.e., into or out of the image, is invisible. Thus, the fault vector components within the *ab*-plane are seen

to be a translation of ½ of a unit cell along a, and a ¼ unit cell along b.

The c-component of the fault can be found by imaging the material along $[100]_o$, shown in Fig. 3(b) (same orientation as Fig. 1(b)). Here, a planar fault again runs vertically through the image, and its presence is demonstrated by the two unit cells marked on either side, with a color scheme applied. The dashed unit cell clearly shows that the bright feature at the centre of the cell (yellow arrow) ends up in a different spot unless the fault is accounted for. In this projection, the $[100]_o$ component of the fault vector cannot be seen, but a shift of ¼ of a unit cell along b agrees with that seen in Fig. 3(a), while there is in addition a shift of ½ unit cell along c. By combining the results in both Figs. 3(a) and 3(b), the full fault vector is therefore established as $\frac{1}{4}[\bar{2}12]_o$, as indicated in both panels. It is worth mentioning again that the ¼ translation along b is used as an appropriate commensurate approximant for the slightly incommensurately modulated structure. Additional atomic resolution STEM imaging was used to confirm the presence of the faults in the $[100]_o$ direction, as shown in Supplemental Material Fig. S3 [18]. Since the same result could be observed using two different techniques across two different microscopes we propose that the presented fault vector determination is accurate.

One consequence of the quarter unit cell component in the fault vector is that there are four translational variants that can exist. That is, each defect in the set of parallel stacking faults in Fig. 2(a) shifts the unit cell by $\frac{1}{4}[\bar{2}12]_o$, only returning to the initial translational variant after four stacking faults are passed. This explains the emergence of the four-fault crossing points in the structure. In order to investigate this aspect further, ISODISTORT was used to decompose the distortions related to the breaking of symmetry from the aristotypical SNN structure *P4/mbm* to the present *Ama2* structure [14,15]. It was found that the relevant order parameter giving rise to the domain structure that emerges as a result of the stacking faults transforms as the irreducible representation of S_3 ($\mathbf{k} = \frac{1}{4}[112]$) of *P4/mbm*, which is related to the rotation of the NbO_6 octahedra in the structure. This order parameter is formally four-dimensional, arising from a 2-dimensional (little) representation S_3 and the two associated arms of the star of $\mathbf{k}$. The two arms of the star of $\mathbf{k}$ correspond to the two possible orthorhombic domains. For a given orthorhombic domain, the four high symmetry OPDs associated with just one arm of the star of $\mathbf{k}$ are illustrated in Fig. 4(a), where the following notation of the permutations is used: $S_3^a = S_3(a, 0; 0, 0)$, $S_3^b = S_3(0, -a; 0, 0)$, $S_3^c = S_3(-a, 0; 0, 0)$, and $S_3^d = S_3(0, a; 0, 0)$. Alternatively, the different OPDs can be viewed as a simple shift of the unit cell, as is also indicated by the vectors written in Fig. 4(a). Importantly, the symmetry of the space group makes these shifts equal to successive shifts along the fault vector $\frac{1}{4}[\bar{2}12]_o$ that was established from the TEM data and described in Fig. 3.

In order to investigate whether or not it is probable for the four OPDs to form the structure of four stacking faults observed experimentally, and where such faults would occur in the structure, the tilting patterns of the NbO_6 octahedra in the OPDs were investigated and compared. It was found that the four OPDs $S_3^a - S_3^d$ form a permutation group (Z_4), where each OPD contains regions in the unit cell where, locally, the tilting pattern does not change when compared to the tilting pattern of the neighboring OPDs. For example, the unit cell of OPD S_3^a contains octahedra that have orientations identical to tilted octahedra in S_3^b, while a different set of octahedra are equivalent when compared to S_3^d. This is illustrated in Fig. 4(b), which is four *Ama2* unit cells wide, the smallest supercell that can capture the 4 faults. The four OPDs have been interfaced to one another—color coded based on the permutations in (a)—with cyan octahedra indicating those octahedra with common tilts. These regions of equivalent octahedra are expected to be low-energy locations for stacking faults in the structure. Importantly, the group of OPDs is cyclical, meaning that no overlap in the tilting pattern of S_3^a and S_3^c, for example, is found. In Fig. 4(c), the pattern of OPDs is also illustrated by their assigned colors across a four-fold stacking fault structure imaged in DF TEM. Here, 2D vectors have been assigned to the different OPDs based on the cyclical nature of the Z_4 permutation group, which forms a pattern reminiscent of a vortex structure or similar topological defect [23]. Since the permutation of the domains (clockwise or anticlockwise) transforms as the permutation group Z_4, which is topologically invariant, we may rigorously describe them as nontrivial topological features.

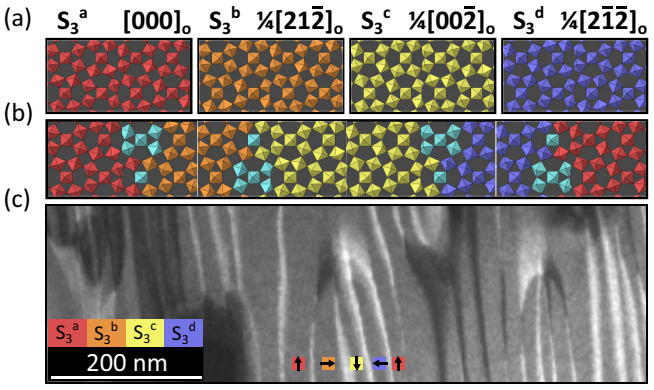

FIG. 4. Fault structure. (a) The four different S_3 OPDs found, where the differences in tilting patterns of the NbO_6 octahedra can be seen. Note that, in order to highlight the octahedral tilting pattern, other order parameters that are needed to fully describe the *Ama2* structure are suppressed in this representation. (b) A superstructure constructed by interfacing the different S_3 OPDs. The cyan octahedra highlight the regions where the tilting pattern is the same for the interfacing OPDs. (c) A DF TEM micrograph, showing several stacking faults. For one set of faults meeting in a four-fold point, colored dots with added 2D vectors are overlaid to indicate a possible arrangement of the OPDs across the domains.

A deeper investigation of the structural model for the stacking faults was carried out through the means of force-field calculations (machine learning from DFT, see Sec. II). Although direct comparisons to similar materials are scarce, DFT calculations on stacking faults in perovskites [24] and semiconductors [25], for example, have shown good correlation with experimental investigations. In the present case, the large size of the unit cell that describes the *Ama2* structure, even before the stacking faults are considered, makes this work particularly challenging. Here, a structure similar to the one presented in Fig. 4(b) was used as a basis for the force-field relaxation, where the goal was to compare the energy

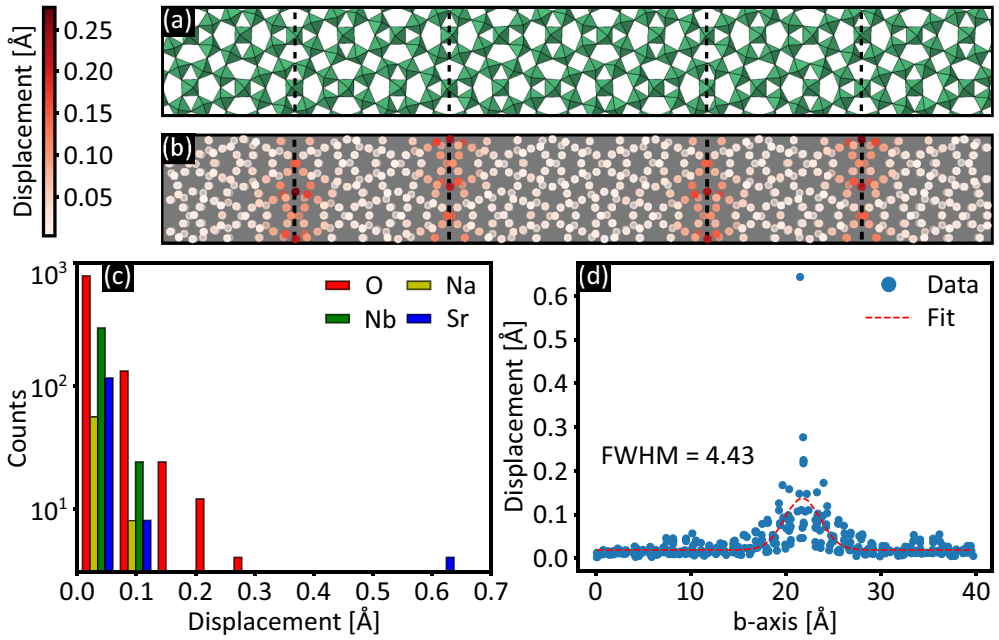

FIG. 5. Results from force-field simulations. (a) The structure after relaxation, here only showing NbO_6 octahedra. Dashed lines indicate the initial placement of stacking faults. (b) Displacement of O atoms for the relaxed structure with respect to the constructed stacking fault structure, where movement is indicated by the color scale and initial stacking fault placement is indicated by dashed lines. (c) Histogram (log scale) illustrating the distribution of absolute atomic displacements. (d) Scatterplot illustrating all atomic displacements across a stacking fault, along with Gaussian fit.

of the structure containing four faults to a basic structure of similar size without faults. In order to encompass the four stacking faults, a supercell consisting of four unit cells along the orthorhombic b-axis was needed, giving a final length of 139.3 Å. The structure presented in Fig. 4(b) is idealised in the sense that only the S_3 order parameter is considered, while the actual structure (and the one used for the force-field calculations) contains additional distortions needed to properly describe the *Ama2* structure of SNN. Furthermore, the structure encompassing the faults was modified to the lower energy *Cc* structure, which the material has been shown to adopt at lower temperatures, since the addition of the faults was expected to break the symmetry of *Ama2* (see Sec. II) [8]. The resulting structure after relaxation is shown in Fig. 5(a), where the initial placement of the stacking faults is indicated by the dashed lines.

In Fig. 5(b), the movement of O atoms during the relaxation of the structure is shown, with magnitude indicated by the color bar. As can be seen, the largest atomic movements are at the stacking faults, suggesting that the initial placement of the faults is a probable low-energy position. The movement of all atomic species is illustrated in a similar way on a unified scale in Supplemental Material Fig. S4 [18]. Figure 5(c) shows the distribution of all atomic movements as a histogram, illustrating that most of the atomic displacements are less than 0.3 Å in magnitude. The exception is a few Sr atoms experiencing displacements of about 0.6 Å. Figure 5(d) shows a quantification of the displacements around one of the faults, along with a Gaussian fit. The fit has a full width at half maximum (FWHM) value of 4.4 Å, giving an estimate of the width of the fault.

The energy difference between the relaxed structure containing four stacking faults compared to a similar *Cc* supercell without faults, ΔE(supercell), was found to be 1.57 eV. Given there are four faults in this supercell, the fault energy per unit area, γ, is $\Delta E(\text{supercell})/(4 \times a_o \times c_o)$, giving $\gamma = 46 \pm 1$ mJ/m (1 eV = 1.602*10-16 mJ, see Supplemental Material [18] for more details on the error estimation). This small energy increase is consistent with the high density of stacking faults observed in SNN, as shown in Fig. 2(a). Such low stacking fault energies are found in, for example, pure metals and alloys [26] (including high entropy alloys [27]) with metallic bonding. In materials with more directional ionic or covalent bonding, low stacking fault energies are only possible when local atomic configurations at the fault are unchanged, for example, in rutile TiO_2 [28] or tetrahedrally bonded semiconductors, including Si [29], and the faults observed here fall into that category. This is not the case for most oxides, including perovskites, which tend to exhibit much larger stacking fault energies [24]. The low stacking fault energy is expected to contribute to the large amount of stacking faults observed in SNN, as shown in Fig. 2(a). The faults occur roughly every 26–29 nm, or about once every 7–8 unit cells along the orthorhombic b-direction (see Supplemental Material Fig. S5 [18]).

The relaxed structure was also compared to the fault-free structure in terms of specific atomic displacements related to the polar nature of the structure. In the *Ama2* setting, the Nb atoms are displaced slightly from the centre of their NbO_6 octahedra along the orthorhombic c-axis, giving the material a polar nature, while in the *Cc* setting, there is an additional polarization along the orthorhombic a-axis. The comparison

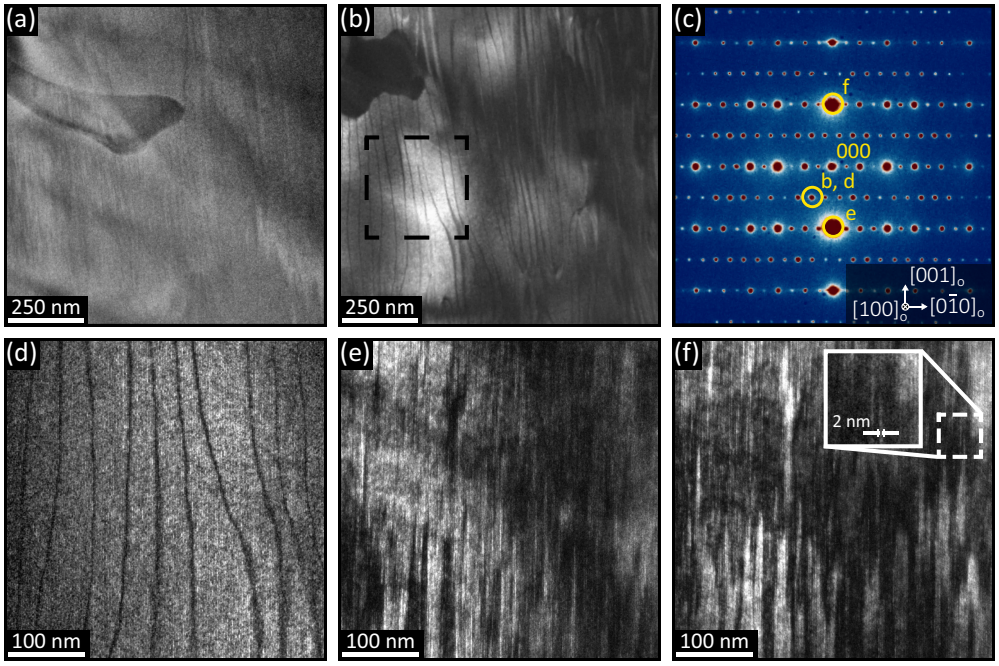

FIG. 6. Investigation of the polarity in SNN. (a) BF and (b) DF of a large area of SNN. (c) Diffraction pattern indicating the spots used for the different imaging conditions. DF patterns highlighting the faults (d), and the extent of opposite polarity (e) and (f), recorded at a higher magnification than (a) and (b).

is shown in Supplemental Material Figs. S6 and S7 and summarized in Table S2 [18]. The displacement of Nb atoms in the relaxed structure within the width of a singular fault is compared to the displacement in the same area of the fault-free structure, revealing a decrease of 32% along the c-axis and an increase of 50% along the a-axis.

A complementary view was revealed through analysis of the symmetry-adapted distortion modes with respect to the aristotype structure. By again cutting up the large supercell with added faults into 20 unit cell-sized slabs (with different origins along the b-axis of the supercell), the structures could be decomposed in ISODISTORT, and specific mode amplitudes could be compared to those of the *Cc* structure without faults. The variation of the Γ_3^- (polarization along c), Γ_5^- (polarization along a), and S_3 (in-plane octahedral tilting) modes is shown in Supplemental Material Fig. S8 and summarized in Table S3 [18]. The averaged amplitude of the Γ_3^- mode across the unit cells decreased by 21% compared to the fault-free *Cc* structure, while the averaged amplitude of the Γ_5^- mode increased by 16%. The comparatively small changes revealed by ISODISTORT are related to the size of the system: here, the polar modes are analysed in a larger region than the small area surrounding the faults, giving a lower magnitude overall. Additionally, the amplitude of the S_3 mode is suppressed across most of the structure, only reaching values seen for the *Cc* structure in the wide regions between faults. This is expected, since the stacking fault structure was constructed from a combination of different OPDs based on the S_3 order parameter, and the faults can be seen as interruptions of the octahedral tilting pattern.

TEM images of TTBs can reveal polar domains as well as stacking faults and twin domains [13], as demonstrated in Fig. 6 for SNN. The bright field micrograph of Fig. 6(a) shows a grain viewed along $[100]_o$ (c-axis vertical). Contrast due to its internal microstructure is faint, but orthorhombic twin domains and stacking faults, similar to those in Fig. 2, are visible. Throughout the image, some additional patches of contrast, corresponding to polar domains, can be observed. This additional contrast is due to the influence of 001 and 00$\bar{1}$ reflections, which have different intensities in regions of different c-polarity.

Dark field images—without the strong background of bright field images—have much better contrast, and can be formed using the different reflections visible in the $[100]_o$ diffraction pattern of Fig. 6(c). Figures 6(d)–6(f) show dark field micrographs of one specific region (marked by a dashed square in Fig. 6(b) using superstructure spots [Figure 6(d)], a 00$\bar{1}$ reflection [Fig. 6(e)] and a 001 reflection [Fig. 6(f)], respectively. In the latter two images, contrast is inverted, indicating a change of polarity along c, i.e., allowing the polar domains in the material to be visualised. They tend to be needle-shaped, with lengths of hundreds of nm along the c-axis while being much narrower along the a-axis (down to the scale of individual unit cells, as shown in the inset of Fig. 6(f)). Notably, there is no correlation between this domain structure and the $\frac{1}{4}[\bar{2}12]_o$ stacking faults in Fig. 6(d) (this was also investigated and confirmed using 4D-STEM, see Supplemental Material Fig. S9 [18]). In agreement with the force-field simulations, the influence of stacking faults is therefore, at most, a small perturbation of the polar irrep Γ_3^-. In fact, c-polar domains are even seen to cross twin boundaries (Supplemental Material Fig. S10 [18]). This, together with the needle-shaped domain structure, suggests that the c-axis displacement of Nb in NbO_6 octahedra is strongly correlated along $[001]_o$ while being relatively insensitive to structural distortions in other directions [8].

IV. DISCUSSION

Here, observations of microstructure, in combination with machine-learned force-field calculations and symmetry mode analysis, have been used to give insight into the stacking fault structure of SNN. Several factors speak to the validity of the structural model used for the calculations: the small magnitude of atomic movements during relaxation and the lack of movement from their original location are both indications of an accurate initial placement of the faults. The estimated stacking fault width of 4.43 Å seems reasonable based on their contrast in HRTEM (Fig. 3) and ADF STEM (Supplemental Material Fig. S3 [18]). This small width justifies the relatively small size of the model (only four unit cells) used for the force-field calculations, which is still large enough for the faults not to overlap or interact directly. It can also explain why the faults do not align with the polar domains: the energy penalty for placing a polar domain wall at the same location is expected to decrease for a wider stacking fault, as the domains formed would be less correlated. Furthermore, the low stacking fault energy of $46 \pm 1\,\mathrm{mJ/m^2}$ estimated from the calculations agrees well with the small width seen, but also the high density of faults observed in TEM (Supplemental Material Fig. S5 [18]).

Based on the force-field calculations, the polarization of the structure was investigated using two complementary methods: analyzing the polar displacement of Nb atoms within NbO_6 octahedra and through symmetry-mode analysis in ISODISTORT. Both methods suggest a decrease in the c-axis polar Γ_3^- mode at the faults (Supplemental Material Figs. S6 and S8 and Tables S2 and S3 [18]), where the displacement analysis gives a more localized value. However, 001 DF TEM images show that correlation of the Γ_3^- mode along the c-axis dominates above all else, with no observable correlation between the polar Γ_3^- domains and stacking faults.

Regarding the Γ_5^- mode, giving in-plane polarization along the orthorhombic a-axis, both Nb displacements and the symmetry mode analysis suggest an increase in the presence of stacking faults (Supplemental Material Figs. S7 and S8 and Tables S2 and S3 [18]). Given the large increase observed in the displacement analysis, the abundance of faults is expected to have a degree of interplay with the low temperature phase transition from *Ama2* to *Cc* (on cooling), related to the in-plane polar instability [8]. However, further analysis specifically targeting the low-temperature phase transition is required in order to prove this connection.

Planar defects similar to those shown here have been described for related TTBs and other functional oxides in earlier studies, where it has also been shown that there is a preference for the faults to meet and annihilate in sets of four [13,30]. The necessity of forming four faults when the displacement vector contains a ¼ in any unit cell direction has also been demonstrated in Ni_3Mo [31]. The meeting points of the faults also show similarities to multiferroic vortex structures such as the "clover-leaf" pattern found in the hexagonal manganates $YMnO_3$ [32] and $ErMnO_3$ [33], and the TTB $CsNbW_2O_9$ [34]. Currently, domain walls, vortices, and other topological structures in ferroelectrics are being investigated for their potential in, for example, memory and logic applications [35,36]. In $YbFeO_3$, the stacking faults act as pinning centres for ferroelectric domains, and therefore, the material on either side of the fault would exhibit inverse polarization [37]. However, as already discussed, there is no such connection between the faults and polar domains in SNN. On the other hand, the fact that the four interfaced S_3 order parameter directions form a cyclical, topologically invariant, Z_4 permutation group, allows us to rigorously describe the domains as nontrivial topological features.

It has also been shown previously that the S_3 order parameter is correlated with the incommensurate modulation along the b-axis of the orthorhombic cell [8]. Since the structure discussed here is constructed from the order parameter directions of S_3, this strengthens the idea that there is a connection between the emergence of stacking faults and the mismatch between the commensurate and incommensurate lattices (see Introduction). A possible route for tuning the ferroelectric properties of these materials is therefore found in controlling the incommensurate modulation, and by extension, the stacking fault density.

V. CONCLUSIONS

In conclusion, stacking faults in $Sr_2NaNb_5O_{15}$ have been thoroughly described based on a combination of transmission electron microscopy imaging, symmetry investigation through ISODISTORT, and machine-learned force-field calculations. The investigation revealed that the stacking faults have a fault vector of $\frac{1}{4}[\bar{2}12]_o$, meet in sets of four, and form domains that can be related as the expression of four directions of the order parameter S_3. This information was then used to construct a probable structure for the force-field calculations, which revealed a minimal stacking fault energy of $46 \pm 1\,\mathrm{mJ/m^2}$. Finally, the analysis of the force-field calculations indicated that the stacking faults have an effect on the polar modes present in the material, with the strongest effect seen for the in-plane polar mode.

ACKNOWLEDGMENTS

The authors would like to thank T. Brown, C. M. King, and S. J. Milne for supplying the SNN ceramic. The authors would like to acknowledge funding from the EPSRC grant "New directions in high temperature dielectrics: unlocking performance of doped tungsten bronze oxides through mechanistic understanding," EP/V053701/1. M.S.S. acknowledges support from the Royal Society (URF/R/231012) for a University Research Fellowship. The authors would also like to thank J. P. Tidey and A. M. Sanchez for fruitful discussions. This work made use of the facilities of the N8 Centre of Excellence in Computationally Intensive Research (N8 CIR) provided and funded by the N8 research partnership and EPSRC (Grant No. EP/T022167/1). The Centre is coordinated by the Universities of Durham, Manchester, and York. This work also made use of the Hamilton HPC Service of Durham University.

DATA AVAILABILITY

There are no publicly available research data or software supporting this manuscript. Requests for further information or data should be sent to the authors.

[1] P. Si, P. Zheng, X. Zhang, C. Luo, X. Zheng, Q. Fan, W. Bai, J. Zhang, L. Zheng, and Y. Zhang, Synergistic modulation of ferroelectric polarization and relaxor behavior of $Sr_2NaNb_5O_{15}$ -based tungsten bronze ceramic, Int. J. Appl. Ceram. Technol. **21**, 532 (2024).

[2] Y. Dan, X. Zheng, Y. Meng, S. Wu, C. Hu, L. Liu, and L. Fang, Simultaneously achieving large energy storage density and high efficiency in the optimized $Sr_2NaNb_5O_{15}$ system with excellent temperature stability at a low electric field, Ceram. Int. **50**, 6801 (2024).

[3] K. Yu, X. Zhang, W. Zhong, P. Zheng, Q. Fan, L. Zheng, Y. Zhang, and W. Bai, Relaxor regulation and enhancement of energy storage properties in bi-modified $Sr_2NaNb_5O_{15}$-based tetragonal tungsten bronze ceramics, J. Mater. Sci. Mater. Electron. **34**, 2069 (2023).

[4] S. Xu, R. Hao, Z. Yan, S. Hou, Z. Peng, D. Wu, P. Liang, X. Chao, L. Wei, and Z. Yang, Enhanced energy storage properties and superior thermal stability in SNN-based tungsten bronze ceramics through substitution strategy, J. Eur. Ceram. Soc. **42**, 2781 (2022).

[5] S. M. R. Billah, Dielectric Polymers, *Functional Polymers* (Springer International Publishing, Cham, Switzerland, 2019), pp. 1–49.

[6] T. Brown, A. P. Brown, D. A. Hall, T. E. Hooper, Y. Li, S. Micklethwaite, Z. Aslam, and S. J. Milne, New high temperature dielectrics: Bi-free tungsten bronze ceramics with stable permittivity over a very wide temperature range, J. Eur. Ceram. Soc. **41**, 3416 (2021).

[7] L. Cao, Y. Yuan, E. Li, and S. Zhang, Relaxor regulation and improvement of energy storage properties of $Sr_2NaNb_5O_{15}$-based tungsten bronze ceramics through B-site substitution, Chem. Eng. J. **421**, 127846 (2021).

[8] J. P. Tidey, U. Dey, A. M. Sanchez, W.-T. Chen, B.-H. Chen, Y.-C. Chuang, M. T. Fernandez-Diaz, N. C. Bristowe, R. Beanland, and M. S. Senn, Structural origins of dielectric anomalies in the filled tetragonal tungsten bronze $Sr_2NaNb_5O_{15}$, Commun. Mater. **5**, 71 (2024).

[9] V. Krayzman, A. Bosak, H. Y. Playford, B. Ravel, and I. Levin, Incommensurate modulation and competing ferroelectric/antiferroelectric modes in tetragonal tungsten bronzes, Chem. Mater. **34**, 9989 (2022).

[10] T. Woike, V. Petříček, M. Dušek, N. K. Hansen, P. Fertey, C. Lecomte, A. Arakcheeva, G. Chapuis, M. Imlau, and R. Pankrath, The modulated structure of $Ba_{0.39}Sr_{0.61}Nb_2O_6$. I. Harmonic solution, Acta Crystallogr. B **59**, 28 (2003).

[11] Y. Ding, J. S. Liu, J. S. Zhu, and Y. N. Wang, Stacking faults and their effects on ferroelectric properties in strontium bismuth tantalate, J. Appl. Phys. **91**, 2255 (2002).

[12] H. Ding, N. Hadaeghi, M. H. Zhang, T. S. Jiang, A. Zintler, L. Carstensen, Y. X. Zhang, H. J. Kleebe, H. B. Zhang, and L. Molina-Luna, Translational antiphase boundaries in $NaNbO_3$ antiferroelectrics, ACS Appl. Mater. Interfaces **15**, 59964 (2023).

[13] G. van Tendeloo, S. Amelinckx, C. Manolikas, and W. Shulin, The direct observation of "discommensurations" in barium sodium niobate (BSN) and its homologues, Phys. Status Solidi **91**, 483 (1985).

[14] H. T. Stokes, D. M. Hatch, and J. Campbell B., ISODISTORT, ISOTROPY Software Suite, Iso.Byu.Edu, http://iso.byu.edu/isodistort.php.

[15] B. J. Campbell, H. T. Stokes, D. E. Tanner, and D. M. Hatch, ISODISPLACE: A web-based tool for exploring structural distortions, J. Appl. Crystallogr. **39**, 607 (2006).

[16] G. Kresse and J. Furthmüller, Efficient iterative schemes for ab initio total-energy calculations using a plane-wave basis set, Phys. Rev. B **54**, 11169 (1996).

[17] R. Jinnouchi, F. Karsai, and G. Kresse, On-the-fly machine learning force field generation: Application to melting points, Phys. Rev. B **100**, 014105 (2019).

[18] See Supplemental Material at http://link.aps.org/supplemental/10.1103/snjy-yzgq for further details on the machine-learned force-fields, processing of HRTEM micrographs, atomic resolution STEM, atomic displacements, fault frequency, polar displacements and symmetry mode analysis, and 4D-STEM, which includes Refs. [19–21].

[19] G. Kresse and D. Joubert, From ultrasoft pseudopotentials to the projector augmented-wave method, Phys. Rev. B **59**, 1758 (1999).

[20] A. P. Bartók and G. Csányi, Gaussian approximation potentials: A brief tutorial introduction, Int. J. Quantum Chem. **115**, 1051 (2015).

[21] A. P. Bartók, R. Kondor, and G. Csányi, On representing chemical environments, Phys. Rev. B **87**, 184115 (2013).

[22] S. C. Chae, N. Lee, Y. Horibe, M. Tanimura, S. Mori, B. Gao, S. Carr, and S. W. Cheong, Direct observation of the proliferation of ferroelectric loop domains and vortex-antivortex pairs, Phys. Rev. Lett. **108**, 167603 (2012).

[23] F. T. Huang, Y. Li, F. Xue, J. W. Kim, L. Zhang, M. W. Chu, L. Q. Chen, and S. W. Cheong, Evolution of topological defects at two sequential phase transitions of $Nd_2SrFe_2O_7$, Phys. Rev. Res. **3**, 023216 (2021).

[24] P. Hirel, P. Marton, M. Mrovec, and C. Elsässer, Theoretical investigation of {110} generalized stacking faults and their relation to dislocation behavior in perovskite oxides, Acta Mater. **58**, 6072 (2010).

[25] M. J. Watts, S. R. Yeandel, R. Smith, J. M. Walls, and P. M. Panchmatia, Atomistic insights of multiple stacking faults in CdTe thin-film photovoltaics: A DFT study, in *2018 IEEE 7th World Conference on Photovoltaic Energy Conversion (WCPEC) (A Joint Conference of 45th IEEE PVSC, 28th PVSEC & 34th EU PVSEC)* (IEEE, Hoes lane, Piscataway, New Jersey, 2018), pp. 3884–3887.

[26] Y. Wang, T. Wang, H. Arandiyan, G. Song, H. Sun, Y. Sabri, C. Zhao, Z. Shao, and S. Kawi, Advancing catalysts by stacking fault defects for enhanced hydrogen production: A review, Adv. Mater. **36**, 2313378 (2024).

[27] T. Z. Khan, T. Kirk, G. Vazquez, P. Singh, A. V. Smirnov, D. D. Johnson, K. Youssef, and R. Arróyave, Towards stacking fault energy engineering in FCC high entropy alloys, Acta Mater. **224**, 117472 (2022).

[28] J. Li *et al.*, Nanoscale stacking fault–assisted room temperature plasticity in flash-sintered TiO_2, Sci. Adv. **5**, eaaw5519 (2019).

[29] R. W. Hertzberg, R. P. Vinci, and J. L. Hertzberg, *Deformation and Fracture Mechanics of Engineering Materials* (John Wiley & Sons Inc., Hoboken, NJ, USA, 2012).

[30] G. van Tendeloo, J. van Landuyt, P. Delavignette, and S. Amelinckx, Compositional changes associated with periodic antiphase boundaries in the initial stages of ordering in Ni_3Mo. I. Crystallographic Analysis, Phys. Status Solidi **25**, 697 (1974).

[31] G. van Tendeloo, P. Delavignette, R. Gevers, and S. Amelinckx, A study of dissociated antiphase boundaries in Ni_3Mo, Phys. Status Solidi **18**, 85 (1973).

[32] M. Lilienblum, T. Lottermoser, S. Manz, S. M. Selbach, A. Cano, and M. Fiebig, Ferroelectricity in the multiferroic hexagonal manganites, Nat. Phys. **11**, 1070 (2015).

[33] M. E. Holtz, K. Shapovalov, J. A. Mundy, C. S. Chang, Z. Yan, E. Bourret, D. A. Muller, D. Meier, and A. Cano, Topological defects in hexagonal manganites: Inner structure and emergent electrostatics, Nano Lett. **17**, 5883 (2017).

[34] S. J. McCartan, P. W. Turner, J. A. McNulty, J. R. Maguire, C. J. McCluskey, F. D. Morrison, J. M. Gregg, and I. Maclaren, Anisotropic, meandering domain microstructure in the improper ferroelectric $CsNbW_2O_9$, APL Mater. **8**, 101108 (2020).

[35] G. F. Nataf, M. Guennou, J. M. Gregg, D. Meier, J. Hlinka, E. K. H. Salje, and J. Kreisel, Domain-wall engineering and topological defects in ferroelectric and ferroelastic materials, Nat. Rev. Phys. **2**, 634 (2020).

[36] J. Seidel, Nanoelectronics based on topological structures, Nat. Mater. **18**, 188 (2019).

[37] G. Ren, P. Omprakash, X. Li, Y. Yun, A. S. Thind, X. Xu, and R. Mishra, Polarization pinning at antiphase boundaries in multiferroic $YbFeO_3$, Chin. Phys. B **33**, 118502 (2024).